# Observation of Enhanced Hot-Electron Production and Strong Shock Generation in Hydrogen-Rich Ablators

Generating strong shocks of up to several hundred megabars makes it possible (1) to explore plasma and material properties at the most-extreme conditions of energy density and (2) to develop two-step inertial confinement fusion (ICF) schemes, where ignition is separated from the main compression of the thermonuclear fuel. A promising two-step ignition scheme is shock ignition (SI),[1–4] where ignition is triggered by a strong shock launched at the end of the implosion and driven by a pressure above ~300 Mbar. Detailed reviews of the current status and physics issues for SI are found in Refs. 5–7. One of the most-critical issues is that the ignitor spike pulse requires a laser intensity of $5 \times 10^{15}$ to $1 \times 10^{16}$ W/cm$^2$, which will excite parametric laser–plasma instabilities (LPI's) in the hot plasma corona surrounding the imploding capsule, thereby transferring a significant amount of the laser energy to the hot electrons. Recent work[8–10] demonstrated that hot electrons can enhance the shock pressure. It is still an open question whether they might preheat a SI target[11] or if the benefits will prevail because the areal density is large enough to stop them in the shell and augment the shock.[12,13] Another concern pertains to the energy coupling. The spike pulse must couple sufficient energy into the target in order to generate a strong-enough shock. LPI's may reduce the coupling efficiency and prevent the seed shock pressure from reaching the required magnitude.

Measuring the pressure at these high intensities directly is nearly impossible, so it must be instead inferred indirectly. Experiments in planar geometry at the Laboratoire pour l'Utilisation des Lasers Intenses (LULI),[14] Omega,[15] and Prague Asterix Laser System (PALS)[16] laser facilities have inferred ablation pressures in the range of ~40 to 90 Mbar, which were limited by lateral heat flow from the laser spots in the planar geometries. The lateral transport was suppressed with the development of a new platform[17,18] that applies spherical targets and x-ray diagnostics. It allows one to evaluate the pressure at shock-ignition–relevant laser intensities. The laser launches an inwardly propagating shock wave that converges at the center, heating a small volume and generating a short x-ray flash that is measured with a time-resolved diagnostic. The shock-launching conditions are inferred by constraining radiation–hydrodynamic simulations to the experimental observables. Several experiments established this scheme as a reliable platform using a variety of laser energies, pulse shapes, and target diameters.

There is a continuing interest in exploring new ablator materials in direct-drive ICF research to improve the hydrodynamic efficiency,[19] mitigate the hot-electron production,[20,21] and suppress the Rayleigh–Taylor instability.[22–24] Recent theoretical work demonstrated an overall better performance with mid-*Z* ablators than plastic (CH) ablators by suppressing the threshold of detrimental LPI while preserving the hydrodynamic stability properties.[25] All of this work has been performed, however, at laser intensities of up to $\sim 1 \times 10^{15}$ W/cm$^2$, which is relevant for the standard hot-spot–ignition concept but not for the spike interaction in shock ignition. No work has been performed so far to study how the ablator material affects the spike interaction.

This article describes for the first time the important role that the ablator material plays in the interaction physics at shock-ignition–relevant laser intensities. We discovered that CH ablators produce significantly more hot electrons than the other materials and show that differences in the hot-electron production influence the shock formation. Instantaneous conversion efficiencies (CE's) of laser energy into hot-electron energy reach ~13% in CH and ~4% in C. According to simulations, hot electrons increase the effective maximum ablation pressure by ~77% in CH and by ~45% in C. This important finding sheds light on the LPI physics in an intensity and plasma regime that is insufficiently explored and might provide a path to higher-energy-density states in direct-drive geometry.

The experiment used 60 UV ($\lambda$ = 351 nm) beams from the OMEGA laser[26] with a total energy of 22 to 26 kJ that were focused to an overlapping beam intensity of up to $\sim 5 \times 10^{15}$ W/cm$^2$ on the surface of a spherical solid target. The beams were equipped with small-spot phase plates,[27] polarization smoothing,[28] and smoothing by spectral dispersion (SSD).[29] Details on the phase-plate configuration can be found in Ref. 18.

The targets with an outer diameter of 412 to 496 $\mu$m consist of an inner CH core that is doped with Ti with an atomic concentration of 5% and an outer ablator layer with a thickness of 20 to 46 $\mu$m of a different material [Fig. 149.26(a)]. The outer layer is irradiated with the laser pulse shown in Fig. 149.26(b). A low-power prepulse of ~1-ns duration produces a plasma corona with which the high-power part of the pulse interacts to generate the shock and the hot electrons.

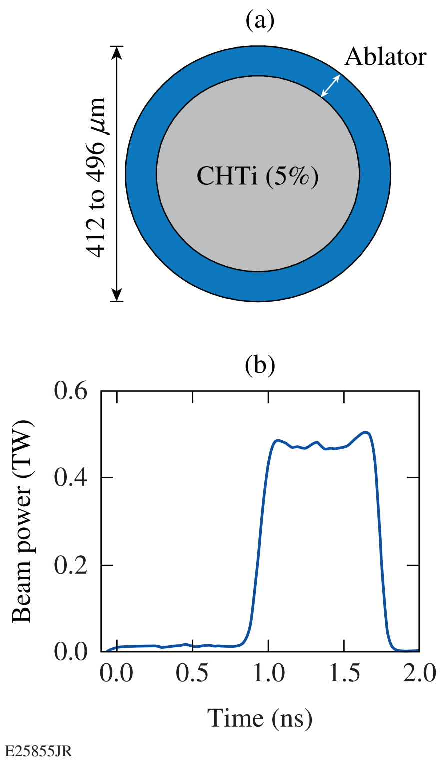


Figure 149.26
(a) Target design consisting of an outer ablator layer of various materials and an inner Ti-doped plastic core; (b) laser pulse shape.

Four different ablator materials (CH, Be, C, and $SiO_2$) with different atomic numbers ($Z$) were used. Table 149.III summarizes the parameters of the ablators. The shock wave converges in the center, which results in a short burst of x-ray radiation that is detected spatially and temporally resolved with multiple x-ray framing cameras. Each framing camera was absolutely timed through dedicated timing shots[19,30] with an accuracy of 30 ps. Time-resolved and time-integrated hard x-ray measurements provide a characterization of the hot-electron population (hot-electron temperature and total energy). Optical backscatter diagnostics measure the amount of absorbed laser energy and the back-reflected laser light.

Figure 149.27(a) shows the measured flash time, which is defined as the occurrence of the x-ray flash relative to the start of the laser pulse, for the different ablators with SSD on (squares) and SSD off (circles) in sequence of increasing $Z$. The measured flash times were adjusted to account for differences in target size, laser energy, and ablator thickness. One-dimensional (1-D) radiation–hydrodynamic simulations were performed with the code *LILAC*[31] to analyze the dependence of the flash time on these variables for each material using the actual measured mass densities. The flash times were then adjusted for an ablator thickness that results in a constant ablator mass, a laser energy of 24 kJ, and a target outer diameter of 430 $\mu$m in order to obtain a valid comparison for the different targets. The data show the general trend of an earlier flash with increasing $Z$ except for CH, which produced the earliest flash. Turning SSD off advances the flash in CH by ~70 ps, while no significant effect is observed in the other materials. Figure 149.27(b) shows the measured time-integrated CE. Plastic stands out by producing by far the most hot electrons with up to ~2 kJ of total hot-electron energy (time-integrated CE ~8%) deposited in the target when SSD was turned off. Nine and seven shots were performed for CH with SSD on and off, respectively, to prove that the observed difference is

Table 149.III: Ablator materials along with the ratio of average mass number and average ionization degree (assuming full ionization), average outer target diameter (OD), average ablator layer thickness, and measured mass density.

| Ablator | $\langle A \rangle / \langle Z_i \rangle$ | ⟨OD⟩ ($\mu$m) | ⟨Thickness⟩ ($\mu$m) | Density (g/cm$^3$) |
|---|---|---|---|---|
| CH | 1.86 | 454 | 40 | 1.04±0.01 |
| Be | 2.25 | 430 | 20 | 1.84±0.01 |
| C | 2.00 | 444 | 28 | 1.4±0.4 |
| $SiO_2$ | 2.00 | 433 | 20 | 1.75±0.2 |

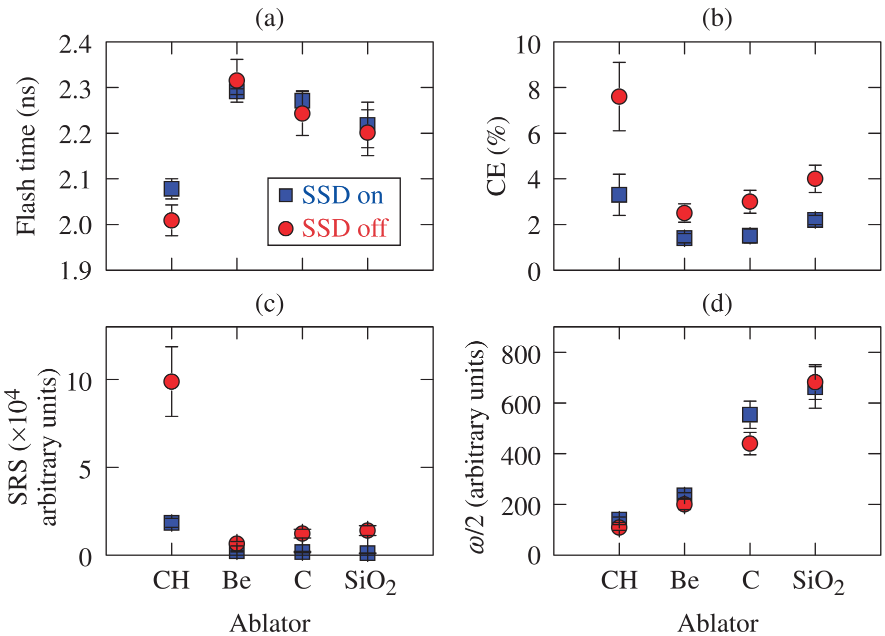


Figure 149.27
(a) X-ray flash time for different ablators with smoothing by spectral dispersion (SSD) on (squares) and SSD off (circles); (b) measured time-integrated conversion efficiency (CE) of laser energy into hot electron energy; (c) stimulated Raman scattering (SRS) backscatter signal; and (d) $\omega/2$ signal.

not an artifact. If CH is treated as an exception, there is the general trend of a slight increase in hot-electron production with higher *Z*. The inferred hot-electron temperatures lie between 60 and 80 keV and are independent of the ablator and SSD. A high hot-electron fraction corresponds to an earlier flash time, which indicates that hot electrons play a role in the shock formation and augment its strength. The experimental data provide information about the dominant mechanism of hot-electron generation. A clear correlation between hot-electron production and the stimulated Raman scattering (SRS) backscatter signal is observed [Fig. 149.27(c)]. Switching SSD on significantly decreases the SRS signal in all ablators, potentially caused by the suppression of beam filamentation. In contrast, the two-plasmon–decay (TPD) instability, which is the other important hot-electron–generation mechanism, is unaffected by SSD and seems to be far less important than SRS in producing hot electrons. The optical emission generated by electron plasma waves (EPW's) with half the laser frequency ($\omega/2$) is much weaker than the SRS emission and monotonically increases [Fig. 149.27(d)] with *Z*.

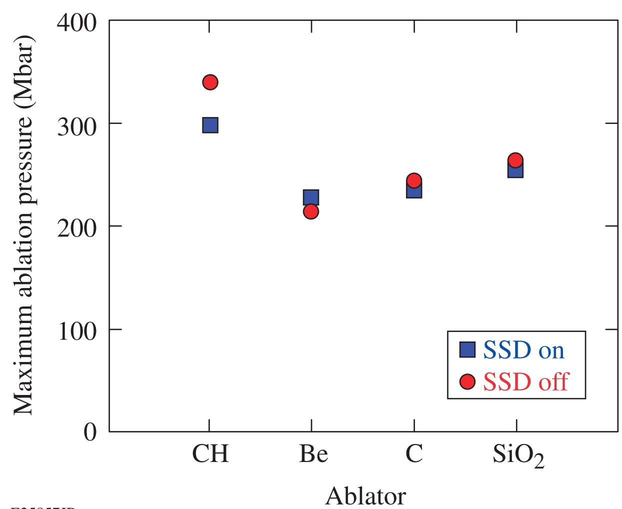


Figure 149.28
Inferred effective maximum ablation pressures for the various materials for an incident laser intensity of $5 \times 10^{15}$ W/cm$^2$.

An effective maximum ablation pressure has been inferred (see Fig. 149.28) from simulations. The effect of hot electrons was taken into account by increasing the flux limiter[32] so that the flash time was recovered in the simulations for each ablator material. Although it has been shown in Ref. 17 that the pressure increase from hot electrons may be described by an increased flux limiter, this simplified description does not capture important details such as slowing down, preheat, and local energy deposition. Additional simulations were performed for the CH target that included a detailed hot-electron transport model, which confirmed the pressures shown in Fig. 149.28.

Figure 149.29 shows the inferred time-resolved CE (red) for two shots with CH (solid) and C (dashed). The blue curves represent the corresponding laser pulse shapes. The onset of hot-electron production lags by ~0.2 ns with respect to the

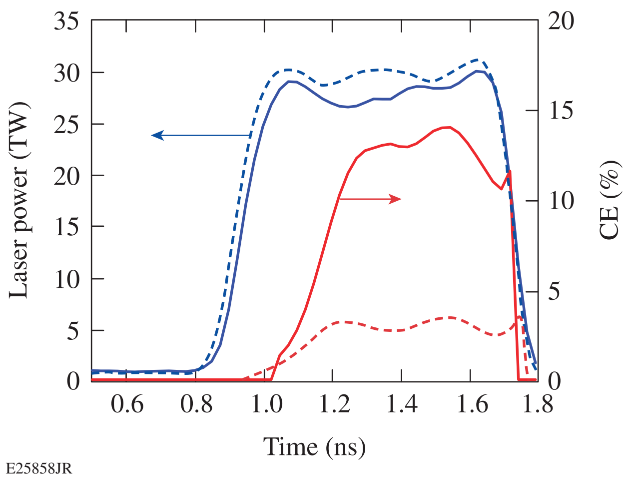


Figure 149.29
Inferred time-resolved conversion efficiency (red) and laser pulse shapes (blue) for two shots with CH (solid curves) and C (dashed curves). Both shots were taken with SSD off. The time resolution of the conversion efficiency is ~100 ps.

rising edge of the laser pulse. This is explained by a strong stimulated Brillouin scattering (SBS) backscatter spike upon the arrival of the main pulse, which reduces temporarily the laser intensity around quarter-critical density $\left(n_c/4\right)$ below the threshold of the SRS and TPD instabilities. In addition, the change in temperature and density scale length in this region also directly affects the LPI thresholds. The development of a plateau in the velocity profile in the region between $n_c/10$ and $n_c/4$ promotes a high SBS gain during this time. After the emission spike with a width of ~0.2 ns, SBS remains about constant on a lower level until the end of the laser pulse. Averaged over the laser pulse shape, SBS scatters back ~2% to 3% of the laser energy with no significant difference between ablators. Time-resolved measurements of the SRS backscattering appear to be closely correlated with the hot-electron production. The time-resolved conversion efficiency is based on the measured time-resolved hard x-ray emission[33] in the photon energy range between 50 and 100 keV. It is assumed that the instantaneous amount of hot electrons is proportional to the instantaneous hard x-ray emission. The conversion efficiencies reached 13±2% and 4±1% in CH and C, respectively, during the second half of the high-intensity pulse, while the time-integrated CE over the whole pulse, including the laser energy when no hot electrons were generated, yielded 9±1% and 3±1% for these shots, respectively.

The amount of hot-electron energy coupled into the target core can be estimated with the technique described in Ref. 34 by using two target types that provide the same corona condition and therefore the same hot-electron source but different core conditions. The differences in hard x-ray emission from a target containing a pure CH core and ablator and the Ti-doped core with CH ablator were compared. About 25% of the hot-electron energy was deposited beyond the ablator layer into the unablated dense target, emphasizing the importance of the energy transport by hot electrons.

The experiments demonstrated significant differences between CH and C ablators, indicating that the H species plays an important role in the LPI. To elucidate the SRS physics, 2-D particle-in-cell (PIC) simulations were performed with the code *OSIRIS*[35] by comparing simulations with and without H in the vicinity of $n_c/4$. A simulation with CH was compared to one where H was removed in the vicinity of $n_c/4$ $\left(n_e > 0.2\, n_c\right)$. These simulations were designed to identify differences in the fundamental physics of SRS caused by the presence of H between CH and C. A boundary with matched density between CH in the underdense portion and pure C in the higher-density portion ensured that equal conditions were created for the laser pulse propagating through the underdense plasma. The input parameters were obtained from a radiation–hydrodynamic simulation for a CH shot evaluated at 1.5 ns when peak hot-electron production was observed. The PIC simulations assumed the same initial plasma parameters. The input thermal electron and ion temperatures were $T_e$ = 4 keV and $T_i$ = 0.8 keV, respectively, and the plasma density ramped linearly from 0.12 $n_c$ to 0.30 $n_c$, slightly above $n_c/4$, with a scale length of 123 $\mu$m. A plane-wave, 351-nm-wavelength laser pulse propagated along the $x$ axis with a nominal intensity of 2.6 × $10^{15}$ W/cm$^2$ (the same intensity as at $n_c/4$ in the implosion), assuming flattop profiles in both time and space. The effect of SSD was not taken into account in the simulation.

Figures 149.30(a) and 149.30(b) show the calculated longitudinal electric field strength from EPW as a function of time and distance along the direction of laser propagation. Distinct differences in the fields are observed. The electromagnetic wave excites strong EPW over a large region in CH compared to C. The wave modes survive longer in CH and couple better with thermal electrons because of a larger **k** vector. As a result, more hot electrons are generated. Figures 149.30(c) and 149.30(d) compare the calculated signal level of ion-acoustic waves (IAW's), showing a stronger damping in CH compared to C because of the presence of light H ions. The calculated CE's into electrons with kinetic energy exceeding 50 keV from the PIC simulations were 12% and 2% for CH and C, respectively. A possible explanation is that the SRS saturation level is controlled by the secondary parametric decay or collapse of the driven plasma wave. The secondary parametric decay has

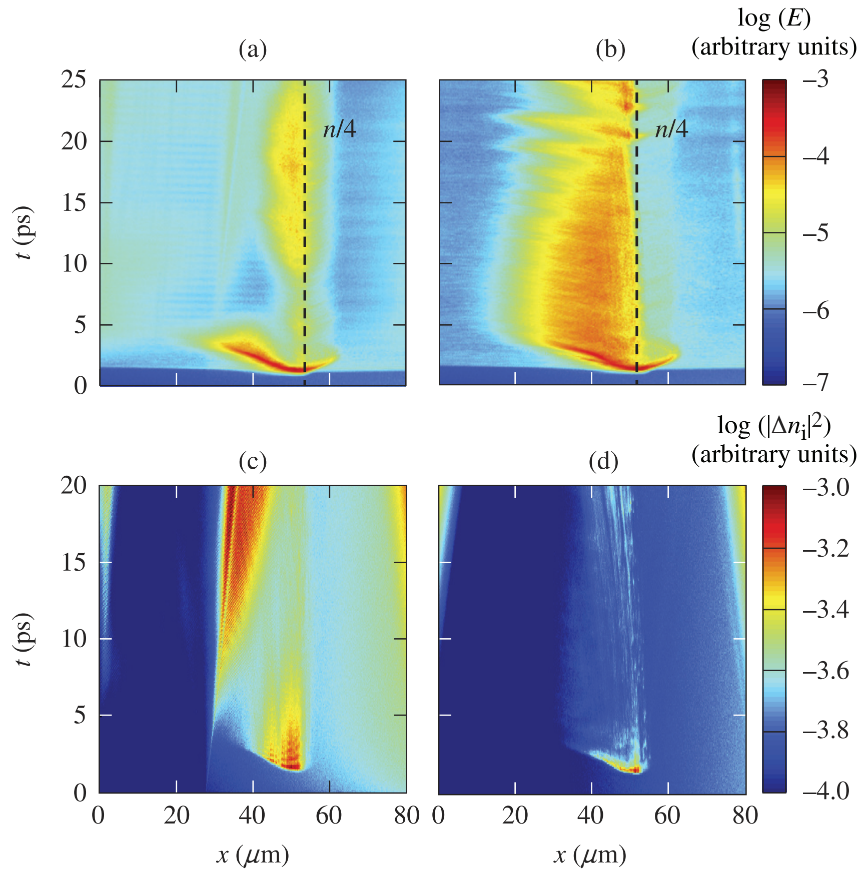


Figure 149.30
Calculated longitudinal electric field strength versus time and space (laser propagates from left to right) for (a) C and (b) CH and calculated ion-acoustic wave level for (c) C and (d) CH. The quantities were averaged over the transversal space coordinate and rendered on a logarithmic scale. The C simulation used a CH layer in the underdense portion, and the pure C layer starts at $x = 30\ \mu$m.

been discussed in many papers; the experimental demonstration was reported in Ref. 36. The threshold of the parametric decay is proportional to the IAW damping rate. In the case of high IAW damping (with H), the threshold is higher and the plasma-wave amplitude can grow to a higher level, producing a stronger SRS signal and a larger number of hot electrons. Conversely, for a small IAW damping, the SRS is saturated by the EPW collapse at a lower level, producing large-scale density modulations and fewer hot electrons. It has been shown theoretically for a fixed $T_e$ and density scale length that a high IAW damping rate promotes higher hot-electron generation;[20] also, theoretical work that studied the nonlinear saturation of SRS in laser hot spots linked an increased SRS reflectivity with a higher IAW damping rate.[37] The observed close correlation between SRS and hot-electron production indicates that IAW damping plays a major role in the CH plasma.

It is expected that the ablator material affects the ablation pressure in various ways. In general, thermal electron-heat conduction is lower in higher-$Z$ materials, and we would expect a reduced mass ablation rate and lower ablation pressure. Based on a simple stationary laser ablation model[38] that neglects radiation and hot electrons, the ablation pressure from thermal transport is given by $p_a = \rho_c^{1/3} I_{abs}^{2/3}$, where $\rho_c$ is the critical mass density and $I_{abs}$ is the absorbed laser intensity. Therefore, the ablation pressure $p_a \sim \left(\langle A\rangle / \langle Z_i\rangle\right)^{1/3}$ depends only weakly on the ratio of mass number and ionization degree for fixed laser wavelength and fixed $I_{abs}$. The expected increase in $p_a$ from CH to Be is only ~7% and even less with respect to the other materials.[19] This experiment demonstrates higher ablation pressures for CH and $SiO_2$, however, indicating that other factors such as hot electrons and potentially radiation transport are more important. Higher-$Z$ materials result in increased collisional absorption and a higher production of x-ray radiation. The radiation impinges deeper into the ablator layer than the thermal electrons, creating a double-ablation front for medium- and high-$Z$ materials.[22,39]

In conclusion, the experiments demonstrate peculiar differences in hot-electron production in the various ablator materials—especially for CH, which generates the most electrons. PIC simulations using input parameters from radiation–hydrodynamic simulations reproduce the higher hot-electron production in CH. This is likely caused by a stronger damping of IAW's in the CH plasma because of the presence of light H ions.

## ACKNOWLEDGMENT

This material is based upon work supported by the Department of Energy National Nuclear Security Administration under Award No. DE-NA0001944, the OFES Fusion Science Center Grant No. DE-FC02-04ER54789, the DOE Laboratory Basic Science Program, the University of Rochester, and the New York State Energy Research and Development Authority. The support of DOE does not constitute an endorsement by DOE of the views expressed in this article. The authors acknowledge the OSIRIS Consortium for the use of *OSIRIS*. R. Y. acknowledges support by the Science Challenge Project of China (No. JCKY2016212A501, No. JCKY2016212A505). Part of this work has been carried out within the framework of the EUROfusion Consortium and has received funding from the European Union's Horizon 2020 research and innovation program under grant agreement number 633053. The views and opinions expressed herein do not necessarily reflect those of the European Commission.

## REFERENCES

1. R. Betti, C. D. Zhou, K. S. Anderson, L. J. Perkins, W. Theobald, and A. A. Solodov, Phys. Rev. Lett. **98**, 155001 (2007).
2. W. Theobald, R. Betti, C. Stoeckl, K. S. Anderson, J. A. Delettrez, V. Yu. Glebov, V. N. Goncharov, F. J. Marshall, D. N. Maywar, R. L. McCrory, D. D. Meyerhofer, P. B. Radha, T. C. Sangster, W. Seka, D. Shvarts, V. A. Smalyuk, A. A. Solodov, B. Yaakobi, C. D. Zhou, J. A. Frenje, C. K. Li, F. H. Séguin, R. D. Petrasso, and L. J. Perkins, Phys. Plasmas **15**, 056306 (2008).
3. X. Ribeyre *et al.*, Plasma Phys. Control. Fusion **51**, 015013 (2009).
4. L. J. Perkins, R. Betti, K. N. LaFortune, and W. H. Williams, Phys. Rev. Lett. **103**, 045004 (2009).
5. S. Atzeni, X. Ribeyre, G. Schurtz, A. J. Schmitt, B. Canaud, R. Betti, and L. J. Perkins, Nucl. Fusion **54**, 054008 (2014).
6. D. Batani, S. Baton, A. Casner, S. Depierreux, M. Hohenberger, O. Klimo, M. Koenig, C. Labaune, X. Ribeyre, C. Rousseaux, G. Schurtz, W. Theobald, and V. T. Tikhonchuk, Nucl. Fusion **54**, 054009 (2014).
7. R. Betti and O. A. Hurricane, Nat. Phys. **12**, 435 (2016).
8. S. Gus'kov *et al.*, Phys. Rev. Lett. **109**, 255004 (2012); X. Ribeyre *et al.,* Phys. Plasmas **20**, 062705 (2013).
9. E. Llor Aisa *et al.*, Phys. Plasmas **22**, 102704 (2015).
10. Ph. Nicolaï *et al.*, Phys. Plasmas **22**, 042705 (2015).
11. A. Colaïtis *et al.*, Phys. Plasmas **23**, 072703 (2016).
12. R. Betti, W. Theobald, C. D. Zhou, K. S. Anderson, P. W. McKenty, S. Skupsky, D. Shvarts, V. N. Goncharov, J. A. Delettrez, P. B. Radha, T. C. Sangster, C. Stoeckl, and D. D. Meyerhofer, J. Phys.: Conf. Ser. **112**, 022024 (2008).
13. K. S. Anderson, R. Betti, P. W. McKenty, T. J. B. Collins, M. Hohenberger, W. Theobald, R. S. Craxton, J. A. Delettrez, M. Lafon, J. A. Marozas, R. Nora, S. Skupsky, and A. Shvydky, Phys. Plasmas **20**, 056312 (2013).
14. S. D. Baton *et al.*, Phys. Rev. Lett. **108**, 195002 (2012).
15. M. Hohenberger, W. Theobald, S. X. Hu, K. S. Anderson, R. Betti, T. R. Boehly, A. Casner, D. E. Fratanduono, M. Lafon, D. D. Meyerhofer, R. Nora, X. Ribeyre, T. C. Sangster, G. Schurtz, W. Seka, C. Stoeckl, and B. Yaakobi, Phys. Plasmas **21**, 022702 (2014).
16. D. Batani *et al.*, Phys. Plasmas **21**, 032710 (2014).
17. R. Nora, W. Theobald, R. Betti, F. J. Marshall, D. T. Michel, W. Seka, B. Yaakobi, M. Lafon, C. Stoeckl, J. A. Delettrez, A. A. Solodov, A. Casner, C. Reverdin, X. Ribeyre, A. Vallet, J. Peebles, F. N. Beg, and M. S. Wei, Phys. Rev. Lett. **114**, 045001 (2015).
18. W. Theobald, R. Nora, W. Seka, M. Lafon, K. S. Anderson, M. Hohenberger, F. J. Marshall, D. T. Michel, A. A. Solodov, C. Stoeckl, D. H. Edgell, B. Yaakobi, A. Casner, C. Reverdin, X. Ribeyre, A. Shvydky, A. Vallet, J. Peebles, F. N. Beg, M. S. Wei, and R. Betti, Phys. Plasmas **22**, 056310 (2015).
19. D. T. Michel, V. N. Goncharov, I. V. Igumenshchev, R. Epstein, and D. H. Froula, Phys. Rev. Lett. **111**, 245005 (2013).
20. J. F. Myatt, H. X. Vu, D. F. DuBois, D. A. Russell, J. Zhang, R. W. Short, and A. V. Maximov, Phys. Plasmas **20**, 052705 (2013).
21. S. X. Hu, D. T. Michel, D. H. Edgell, D. H. Froula, R. K. Follett, V. N. Goncharov, J. F. Myatt, S. Skupsky, and B. Yaakobi, Phys. Plasmas **20**, 032704 (2013).
22. S. Fujioka *et al.*, Phys. Plasmas **11**, 2814 (2004).
23. A. N. Mostovych, D. G. Colombant, M. Karasik, J. P. Knauer, A. J. Schmitt, and J. L. Weaver, Phys. Rev. Lett. **100**, 075002 (2008).
24. G. Fiksel, S. X. Hu, V. N. Goncharov, D. D. Meyerhofer, T. C. Sangster, V. A. Smalyuk, B. Yaakobi, M. J. Bonino, and R. Jungquist, Phys. Plasmas **19**, 062704 (2012).
25. M. Lafon, R. Betti, K. S. Anderson, T. J. B. Collins, R. Epstein, P. W. McKenty, J. F. Myatt, A. Shvydky, and S. Skupsky, Phys. Plasmas **22**, 032703 (2015).
26. T. R. Boehly, D. L. Brown, R. S. Craxton, R. L. Keck, J. P. Knauer, J. H. Kelly, T. J. Kessler, S. A. Kumpan, S. J. Loucks, S. A. Letzring, F. J. Marshall, R. L. McCrory, S. F. B. Morse, W. Seka, J. M. Soures, and C. P. Verdon, Opt. Commun. **133**, 495 (1997).
27. S. P. Regan, T. C. Sangster, D. D. Meyerhofer, W. Seka, R. Epstein, S. J. Loucks, R. L. McCrory, C. Stoeckl, V. Yu. Glebov, O. S. Jones, D. A. Callahan, P. A. Amendt, N. B. Meezan, L. J. Suter, M. D. Rosen, O. L. Landen, E. L. DeWald, S. H. Glenzer, C. Sorce, S. Dixit, R. E. Turner, and B. MacGowan, J. Phys.: Conf. Ser. **112**, 022077 (2008).
28. T. R. Boehly, V. A. Smalyuk, D. D. Meyerhofer, J. P. Knauer, D. K. Bradley, R. S. Craxton, M. J. Guardalben, S. Skupsky, and T. J. Kessler, J. Appl. Phys. **85**, 3444 (1999).
29. S. Skupsky, R. W. Short, T. Kessler, R. S. Craxton, S. Letzring, and J. W. Soures, J. Appl. Phys. **66**, 3456 (1989).
30. D. T. Michel, A. K. Davis, W. Armstrong, R. Bahr, R. Epstein, V. N. Goncharov, M. Hohenberger, I. V. Igumenshchev, R. Jungquist, D. D. Meyerhofer, P. B. Radha, T. C. Sangster, C. Sorce, and D. H. Froula, High Power Laser Science and Engineering **3**, e19 (2015).

31. J. Delettrez, R. Epstein, M. C. Richardson, P. A. Jaanimagi, and B. L. Henke, Phys. Rev. A **36**, 3926 (1987).

32. R. C. Malone, R. L. McCrory, and R. L. Morse, Phys. Rev. Lett. **34**, 721 (1975).

33. C. Stoeckl, R. E. Bahr, B. Yaakobi, W. Seka, S. P. Regan, R. S. Craxton, J. A. Delettrez, R. W. Short, J. Myatt, A. V. Maximov, and H. Baldis, Phys. Rev. Lett. **90**, 235002 (2003).

34. A. R. Christopherson, R. Betti, W. Theobald, C. J. Forrest, E. M. Campbell, J. Howard, J. A. Delettrez, C. Stoeckl, D. H. Edgell, W. Seka, V. Yu. Glebov, A. K. Davis, A. Bose, A. V. Maximov, M. S. Wei, and J. Peebles, "Direct Measurements of Hot-Electron Preheat in Inertial Confinement Fusion Implosions," to be submitted to Physical Review Letters.

35. R. A. Fonseca *et al.*, in *Computational Science—ICCS 2002*, edited by P. M. A. Sloot *et al.*, Lecture Notes in Computer Science (Springer, Berlin, 2002), Vol. 2331, pp. 342–351.

36. S. Depierreux *et al.*, Phys. Rev. Lett. **84**, 2869 (2000).

37. D. A. Russell, D. F. DuBois, and H. A. Rose, Phys. Plasmas **6**, 1294 (1999).

38. W. M. Manheimer, D. G. Colombant, and J. H. Gardner, Phys. Fluids **25**, 1644 (1982).

39. J. Sanz, R. Betti, V. A. Smalyuk, M. Olazabal-Loume, V. Drean, V. Tikhonchuk, X. Ribeyre, and J. Feugeas, Phys. Plasmas **16**, 082704 (2009).